

# Plexus Convolutional Neural Network (PlexusNet): A novel neural network architecture for histologic image analysis

Okyaz Eminaga, Mahmoud Abbas, Christian Kunder, Andreas M. Loening, Jeanne Shen, James D. Brooks, Curtis P. Langlotz, and Daniel L. Rubin

**Abstract**— Different convolutional neural network (CNN) models have been tested for their application in histologic imaging analyses. However, these models are prone to overfitting due to their large parameter capacity, requiring more data and expensive computational resources for model training. Given these limitations, we developed and tested PlexusNet for histologic evaluation using a single GPU by a batch dimension of  $16 \times 512 \times 512 \times 3$ . We utilized 62 Hematoxylin and eosin stain (H&E) annotated histological images of radical prostatectomy cases from TCGA-PRAD and Stanford University, and 24 H&E whole-slide images with hepatocellular carcinoma from TCGA-LIHC diagnostic histology images. Base models were DenseNet, Inception V3, and MobileNet and compared with PlexusNet. The dice coefficient (DSC) was evaluated for each model. PlexusNet delivered comparable classification performance (DSC at patch level: 0.89) for H&E whole-slice images in distinguishing prostate cancer from normal tissues. The parameter capacity of PlexusNet is 9 times smaller than MobileNet or 58 times smaller than Inception V3, respectively. Similar findings were observed in distinguishing hepatocellular carcinoma from non-cancerous liver histologies (DSC at patch level: 0.85). As conclusion, PlexusNet represents a novel model architecture for histological image analysis that achieves classification performance comparable to the base models while providing orders-of-magnitude memory savings.

**Index Terms**— Machine learning, Medicine and science, Image Processing and Computer Vision, and Diagnostics

## 1 INTRODUCTION

Management of patients with cancer disease requires a reliable pathological evaluation. Any pathological examination begins with an initial evaluation of tumor extent. However, the limitation of human resources, the increased documentation procedures, and the cost pressure in the health care force pathologists to shorten their evaluation phase by focusing on capturing the most relevant findings, while maintaining their concentration for histological tumor detection. Given the obstacles in clinical routine and the recent advance in computational efforts and methodologies, computer-aided solutions have shown the potential for an accurate cancer detection from histologic images using advanced machine learning approaches and algorithms related to computer vision [1-8]. Convolutional neural networks have been frequently used for cancer

detection on histologic images. Different convolutional neural network (CNN) models have been introduced and tested for their ability to classify histological images, such as in distinguishing regions of normal and cancerous cells [1-6]. To date, most studies on histologic imaging have utilized U-Net [9], VGG16 [10], Inception V3 [11], ResNet [12], DenseNet [13] for segmentation and classification problems [2, 14-18]. These models are based on linear non-parallel architecture systems. However, a major limitation of these models is the large number of parameters (in the millions) that require large data sets and significant computational resources for model training and validation, and the risk for overfitting by insufficient data amount.

For that reason, we have developed a novel condensed deep learning architecture that requires significantly fewer parameters, fewer hardware resources and larger tiles of the whole-slide images, while maintaining the classification performance. Given the excellent performance of this deep learning model when run on affordable hardware, we provide a trainable system that can be deployed for histological identification of cancer on histologic images and can be optimized for clinical applications in the pathology suite, such as initial automated screening of biopsy samples or post-surgical samples.

## 2 RELATED WORK

Lijten et al introduced first a neural network architecture to identify histological prostate cancer on biopsy samples [8]. A recent study by Campanella et al. also utilized the a large-sized biopsy samples to introduce a multiple instance learning-based deep learning system based on

- O.E is with the Center for Artificial Intelligence in Medicine & Imaging, DeepMedicine.ai, and Department of Urology, Stanford School of Medicine, Stanford, CA 94305. E-mail: okyaz.eminaga@stanford.edu.
- M.A. is with the Institute for Pathology and Cytology, Schüttorf, 48465, E-mail: mahabbas74@googlegmail.com.
- C.K. is with the Department of Pathology, Stanford School of Medicine, Stanford, CA 94305. E-mail: ckunder@stanford.edu.
- A.M.L. is with the Department of Radiology, Stanford School of Medicine, Stanford, CA 94305. E-mail: loening@stanford.edu.
- J.S. is with the Center for Artificial Intelligence in Medicine & Imaging and Department of Pathology, Stanford School of Medicine, Stanford, CA 94305. E-mail: jeannes@stanford.edu.
- J.D.B. is with the Department of Urology, Stanford School of Medicine, Stanford, CA 94305. E-mail: jbrooks1@stanford.edu.
- C.P.L. is with the Center for Artificial Intelligence in Medicine & Imaging, Stanford School of Medicine, Stanford, CA 94305. E-mail: langlotz@stanford.edu
- D.L.R. is with the Department of Biomedical Data Science, Stanford School of Medicine, Stanford, CA 94305. E-mail: rubin@stanford.edu

ResNet [7]. Other studies have also used the state-of-art neural networks for identifying regions of histological cancer on TCGA datasets for prostate cancer [1-6]. However, these methods require expensive computation resources (e.g. multiple GPUs or expensive computational cloud solutions) and are often limited to using small patch images to overcome the hardware limitations. Use of small patch images results in smaller grids of the whole-slide images, thereby decreasing the review window and data flow at the given processing time of whole slice images. Finally, these models were developed for classification problems broadly, and not specifically designed from the specific problem of classifying histological features. Histology images belong to a specific classification domain in that they are highly granular and utilize a specific range of features for classification. Our goal was to develop a novel CNN architecture tailored to the specific needs of histological discrimination of cancer from non-cancer, thereby taking the potential of having limited computational resources into account.

### 3 PLEXUS CONVOLUTIONAL NEURAL NETWORK

The components of the plexus neural network (Alias: PlexusNet) include: the normalization section, feature extraction section and the classification section. The normalization section is optional, whereas the feature and classification sections are mandatory. The standard activation function for the 2D convolutional layers and the fully connected layer is the rectified linear unit. Figure 1 illustrates the major components of PlexusNet.

#### 3.1 Color intensity normalization section

We considered the color intensity normalization as a vector problem with a global angle displacement. The normalization is realized as follows: Given that an image raster is a tensor with red, green and blue channels (RGB), all color channels were divided by 255 in order to have the pixel value between 0 and 1 for each color channel and performed vector calculation using the formula that is inspired by steerable filters [19]:

$$-2 \cos(90 \omega_1) e^{-(2x^2)} - 2x \sin(90 \omega_2) e^{-(2x^2)} \quad (1)$$

where  $\omega_1$  and  $\omega_2$  are the weights required for the angle determination that have values that range between 0 and 1, and where  $x$  is the image raster.  $\cos(90 \omega_1)$  and  $\sin(90 \omega_2)$  terms are the corresponding interpolation functions for  $-2e^{-(2x^2)}$  and  $-2xe^{-(2x^2)}$ , respectively. The optimal weights for calculating the optimal angle were determined during the training procedure. After that, the values were scaled between -1 and 1 using the formula:

$$2((X - \min(X)) / (\max(X) - \min(X))) - 1 \quad (2)$$

After applying the normalization algorithms, the tensor was fed into a convolution layer with a batch normalization step that adjusts and scales the activations of the convolution layer [20]. Further, this layer generates multiple channels and reduces the tensor dimension by half using a

filter size of 16 and a kernel size of  $5 \times 5$  pixels with a stride of 2 pixels. Here, the kernel size was defined arbitrary and filter size was set to the batch size.

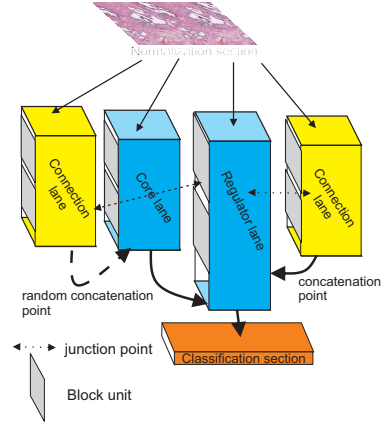


Fig. 1. The general components of PlexusNet that consists of 3 sections: the normalization section, the feature extraction section, and the classification section. The feature extraction section consists of multiple lanes. Each lane consists of block units (Figure 2). The core lane is responsible for generating feature-maps and maintaining the data transmission from the normalization section to the classification section, whereas the connection lane, the regulator lane and the junction point regulate the data transmission through the network. The connection lanes interact with the core lanes by concatenating the feature-maps at certain block level determined either by the user or randomly to influence the learning process of each lane. The junction point (the junction weighted layer) aims to weigh the relevance of the feature maps of core lane for the classification problem compared to the regulator lane and to transfer the relevant features through the core lane.

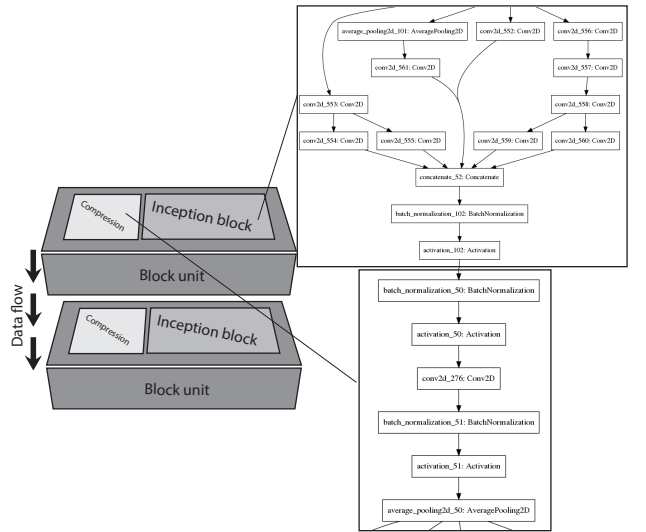


Fig. 2. describes the components of a lane. A lane consists of multiple blocks units. Each block units consists of the feature extraction segment (Inception block) and the compression segment. The feature extraction segment can be an inception block or any type of blocks. "conv2d": 2D convolution layer, "average\_pooling2d": Average pooling layer, "concatenate": concatenation layer, "batch\_normalization": Batch normalization, and "activation": Activation function (Default: rectified linear unit). Supplement code file 1 illustrates the implementation of the block unit.

### 3.2 Feature extraction section

In order to force the model to extract the most meaningful features from the normalized tensors, we introduced unique regulatory mechanisms for feature extraction and data flow inspired by observations in neuroscience in which cells in a neural ganglion interact with other components of the nervous system in the spine that process signals and regulate the flow of signals from multiple channels between the peripheral and central nervous system.

The plexus structure of the feature extraction section consists of the connection lanes, core lanes, junction points and a regulator lane. Each lane is a sequence of blocks as shown in Figure 2. The number of blocks defines the lane depth as a way to regulate the depth of the feature extraction process. Each block contains a feature extraction segment and feature compression segment. The feature extraction segment can be an inception block or any custom block architecture. The feature compression segment reduces the channel number of the feature tensors for the purposes of dimension reduction and preservation of relevant information. The compression rate regulates how much information each block contributes to the global state. The supplement code file 1 provides an example of the block unit.

The core lane is responsible for generating feature-maps and maintaining the data transmission from the normalization section to the classification section, whereas the connection lane, the regulator lane and the junction point regulate the data transmission through the network. The connection lanes interact with the core lanes by concatenating the feature-maps at certain block level determined either by the user or randomly to influence the learning process of each lane. The junction point (the junction weighted layer) aims to weigh the relevance of the feature maps of core lane for the classification problem compared to the regulator lane and to transfer the relevant features through the core lane as given in the formula:

$$J_j = (\theta_{1j}\mathcal{R}_j) + (\theta_{2j}\mathcal{C}_j) \quad (3)$$

where  $\theta_1$  and  $\theta_2$  are the weights,  $\mathcal{R}$  is a feature map from the regulator lane,  $\mathcal{C}$  is a feature map from the core lane at block level  $j$ .  $J_j$  is the output of the junction weighted layer.

The regulator lane is a special condition of the core lane that regulates the feature extraction in other core lanes through the junction points and the last concatenation layer of the feature extraction section.

The main difference between the connection lane and the core lane is that the connection lanes end in the middle of the plexus by merging to the next right core lane that has a junction point with the regulator. The connection lane is shorter than the core lane, its block number depends on the location of the merging level between these lanes. In the final layer of the feature extraction section, all core lanes and the regulator lane are concatenated as preparation for the next fully connected layers in the classification section. Overall, the architecture of PlexusNet is inspired by the neuroanatomy [21]. A core lane represents one of the major spine tracts inside the spine that are spanned from the periphery (Input data and normalization section) to the brain (classification section) and responsible for signal

processing and signal transferring. Connection lanes are ganglion nerves that are located inside the spine, regulate the signal flows inside the spine, and usually connected to other spine tracts and don't have a direct connection to the brain. The regulator lane represents the regulative spinal tract like extrapyramidal tracts that has connections between periphery and brain and regulates the signal flow and its intensity.

### 3.3 Classification section

After concatenation of the feature maps from all core lanes, global pooling was used to reduce feature dimensions to a one-dimensional array with a length equal to the channel number of all core lanes. The feature-array is fed into a fully-connected layer which is then connected to a classification layer that is defined by an activation function and the number of the classification.

The current study used "softmax" for the final activation function of the last fully connected layer by one-hot-encoding of the tumor presence status.

### 3.4 Hyperparameters

We defined the hyperparameters to reconstruct the plexus neural network and provided default values for these parameters as follows.

1. The initial filter of the first layers; this parameter is required to calculate the filter size of the consecutive layers. (Default value: 2, higher value may require more GPU memory)
2. The number of core lanes, which is essential to generate the main structure of the plexus; the minimum number allowed is 2. (Default value: 5)
3. The index of the regulator lane; the default value is set at 0.
4. The number of the junction points and their coordination. The number of the junction points is equal to the number of the connection lanes. The coordination of junction points consists of the index of the regulator lane and the index of the next core lane that can be either randomly defined or given as hyperparameter. Further, the block level at which the junction point occurs can either be determined randomly or specified as hyperparameter. (Default value: 3)
5. The concatenating block level between the connection lane and the core lane. By default, the merging block level is defined randomly, but can be modified by providing the block level and the indices of the corresponding connection and core lanes.
6. The activation regularization which is optional and can be L1 or L2 regularization. (Default value: None)
7. The architecture of the block unit; by default, the block architecture is inception. The user can modify the block architecture as needed.
8. The block compression rate, which reduces the channel number of the feature tensors from the feature extraction part of the block by a given rate. (Default value: 0.5)
9. The number of classes ( $n=2$ ) and the last activation.

We evaluated the effectiveness of PlexusNet on the task of classifying prostate and liver cancer histology datasets and compared classification performance with 4 state-of-the-art neural network architectures: DenseNet, MobileNet, NASNetMobile, and Inception V3. Moreover, we evaluated the effect of different hyperparameter configurations on the classification performance of PlexusNet.

## 4 HISTOLOGY IMAGES

### 4.1 Prostate Cancer

The study cohort for prostate cancer consists of 62 whole-slide images randomly selected from TCGA dataset (TCGA-PRAD,  $n=54$ ) and from the prostate cancer image database at Stanford Medical School ( $n=8$ ). Information related to the distribution of tumor stage and Gleason score are given in Supplement Table 1. The histology slides were obtained from formalin-fixed paraffine-embedded (FFPE) tissue blocks from patients who underwent total removal of the prostate as part of the treatment of the prostate cancer. These slides were stained with hematoxylin and eosin staining (H&E) and scanned using Aperio Digital Pathology Slide Scanners from Leica Biosystem (Wetzlar, Germany). TCGA images were scanned at 40x magnification, whereas those from Stanford were scanned at 20x. Digital images were stored in SVS format. The tumor areas for TCGA datasets were annotated by OE and MA, whereas Stanford images were annotated by CK using the software Aperio Image Scope from Leica Biosystem (Wetzlar, Germany). CK, MA are senior pathologist with a strong background in genitourinary pathology (CK: 4 years clinical experience, MA: > 10 years clinical experience) and OE is a urologic consultant and medical scientist with long research experience in prostate cancer pathology (10 years). For the model evaluation, we considered TCGA images as the training set and Stanford images as the validation set. More details regarding performance measurement of model can be found in the section “evaluation metrics”.

### 4.2 Hepatocellular Carcinoma

Twenty-four whole-slide H&E images were obtained from TCGA dataset (TCGA-LIHC diagnostic), which are originated from FFPE blocks of liver tissues from 24 patients who were diagnosed with hepatocellular carcinoma. These H&E images were scanned at 40x using scanners provided by Leica Biosystem (Wetzlar, Germany). The tumor regions were manually outlined by JS who is a senior pathologist with subspecialty expertise in gastrointestinal and liver pathology (> 10 years clinical experience). For the model evaluation, the images were randomly split into 19 images for the training set and 5 images for the validation set. Supplement Table 2 provides information related to the frequencies of tumor stages and tumor grading in the study cohort.

### 4.3 Generation of patch images

For the definition of the coordinate grid for the patch image generation, the highest (lowest magnification) level of the SVS image for the whole-slide image was considered and converted to a gray-scale image. Then, the tissue region was masked by thresholding by the mean value of the

gray intensity. To determine the coordination of each patch image, the default size of patch image (512x512 pixels) was rescaled after dividing by scale factors for height and width. These scale factors were determined by calculating the ratio of the dimension of the whole-slide image at 10x to the image dimension of the highest level. Further, the overlapping ratio of 0.2 was applied for overlapping two neighboring patch images in vertical direction. Patch images not covered by masked tissue region were excluded to remove background images from the dataset. Finally, the grid for patch images was upsampled by multiplying by the scale factors. All histologic images were finally tiled by 512x512 pixels (330x330  $\mu\text{m}$ ) at 10x magnification level based on the given coordination from the grid. The 10x magnification level was considered based on the clinical experience of pathologists [22, 23]. The average number of patch images from prostate cancer was 979 [95% Confidence Interval (CI): 773 – 1,184]. The ground truth was considered as a binary mask generated from the annotation data (Spatial information and closed polygon points) for prostate cancer or hepatocellular carcinoma in each slide image. The binary mask has the dimension of the original image in order to maintain the same resolution. The patch mask was extracted at the same location of the corresponding patch image. The percentage of positive pixels to the patch image size was estimated to classify each patch image for the presence status of tumors. A patch image is positive if the number of positive pixels meets or exceeds a threshold of 20%, which is an approximated mean of the positive pixels of the training set. From histology images with hepatocellular carcinoma, 973 patch images were generated from each slide in average (95% CI: 764 – 1,182) using the same approach. For models other than PlexusNet we applied CLAHE (Contrast Limited Adaptive histogram equalization) to optimize the contrast of the patch images as this approach has shown an improvement the feature extraction [24]. CLAHE was not applied for PlexusNet as the color intensity normalization is one component of PlexusNet.

## 5 MODEL TRAINING AND EVALUATION

Eleven PlexusNet models with different hyperparameter configurations were developed and evaluated. The hyperparameter configuration for each model is listed in Table 1. An example of the model structures is provided as Supplement file 1. To evaluate the effect of the composition of the development set on the model performance, we defined two scenarios for the composition of the development set using the prostate dataset. The first scenario considered all histology images from TCGA-PRAD and Stanford University, from which tiles were generated and randomly assigned either to the training set or the validation set. The second scenario defined all histology images from TCGA-PRAD as training set and the Stanford’s histology images as validation set. We tested these scenarios on PlexusNet models with different configurations and compared the performance of the state-of-art models with that of PlexusNet (Model 1) in each scenario. For the first scenario, we had 49,179 patch images for training (89%) and 6,064

patch images for validation (11%). For the second scenario, 48,616 (88%) patch images were generated for training and 6,627 (12%) for validation set. For the classification of hepatocellular carcinoma, the training set consisted of 20,456 patch images (88%) and the validation set had 2,786 patch images (12%). From the validation set, 10% patch images from each slide was randomly selected and used as a validation set for the model development. The remaining 90% patch images were reserved as internal validation for top models.

These models were trained and validated on the prostate cancer dataset without applying any image augmentation which has been found to have a regularization effect on the model training to reduce the overfitting risk [25]. Due to the high-probability of overfitting in the first scenario, we limited our comparison analysis between the state-of-art models and PlexusNet model to the first 5 epochs. For other conditions, we stopped our model training after 10 epochs.

For hepatocellular images, we randomly applied the horizontal and/or vertical flipping, and/or the image rotation of patch images for the purpose of image augmentation since we utilized hepatocellular images to prove the generalization of PlexusNet. The PlexusNet model (Model 1) and other state-of-the-art models were trained until the 15<sup>th</sup> epoch.

All models were trained using the optimization algorithm ADAM. In addition, the Yogi optimization approach was used for training PlexusNet since this algorithm is designed for non-convex-optimization [26]. The loss function “categorical cross entropy” was applied for models. The initial learning rate was set to 1e-3 (1e-4 for hepatocellular carcinoma) and was reduced exponentially by multiplying by 0.9 after every 5 epochs. All models with the exception of DenseNet (batch size = 8) were trained using a batch size of 16 patch images. During the training, we measured the classification accuracy, the categorical cross-entropy loss and the dice coefficient for each step. The validation evaluation was performed after each training epoch, and the evaluation metrics were registered and stored in a csv file.

### 5.1 Evaluation metrics

The evaluation metrics for the accuracy of tumor classification were the classification accuracy and dice coefficient (DSC) at a threshold of 0.5 for the likelihood rate for cancer presence in each patch image. We evaluated these deep learning models patch-wise. Further, the loss values from the training and validation set were compared between the models. All models were trained on the training set and validated on the validation set. A comparison analyses of evaluation metrics between different models in a given epoch window were performed using ANOVA with post-hoc Tukey HSD (Honestly Significant Difference) at 95% confidence intervals and the P-values were adjusted using Tukey’s method. Adjusted P-values below 0.2 were considered significant for two-tiled tests. After evaluating the classification performance for models representing different types of neural network architecture, the top three models were evaluated on the internal validation set at the slide level using DSC and by calculating the area under the

curve (AUC).

Our analyses were performed using Python 3.6 (Python Software Foundation, Wilmington, DE) and applied the Keras library that is built-on the TensorFlow framework, to develop the models. R (R Foundation for Statistical Computing, Vienna, Austria) was used for post-hoc analysis. All analyses were performed on a GPU-containing machine with an Intel processor with 32 GB RAM (Intel, Santa Clara, CA), 2 TB PCIe flash memory, 5 TB Hard disk, and NVIDIA GeForce Titan Xp with 11 GB VRAM. The code script for metric evaluation is publicly available (Github: <https://github.com/oeminaga/PlexusNet.git>).

## 6 RESULTS

The models for prostate cancer detection were trained and evaluated on patch images, where 35.4% of patch images classified as tumor. The eleven models representing different hyperparameter configurations of the models revealed that the amplitudes of loss curves in the first 5 epochs are most intensive followed by reduction of the amplitudes or by developing a plateau for most models (Figure 3). However, the volatility of loss values remained after 5th epoch for models 5 and 8, revealing the importance of the junction number on stabilizing the loss course. Figure 3 revealed that the models 8 to 11, which have reduced junction numbers, had a very volatile loss curve in the first 5 epochs, while the loss curve of model 7 was less volatile in the last 5 epochs, compared to other models having lesser number of junction points. The best Dice-coefficient (DSC)

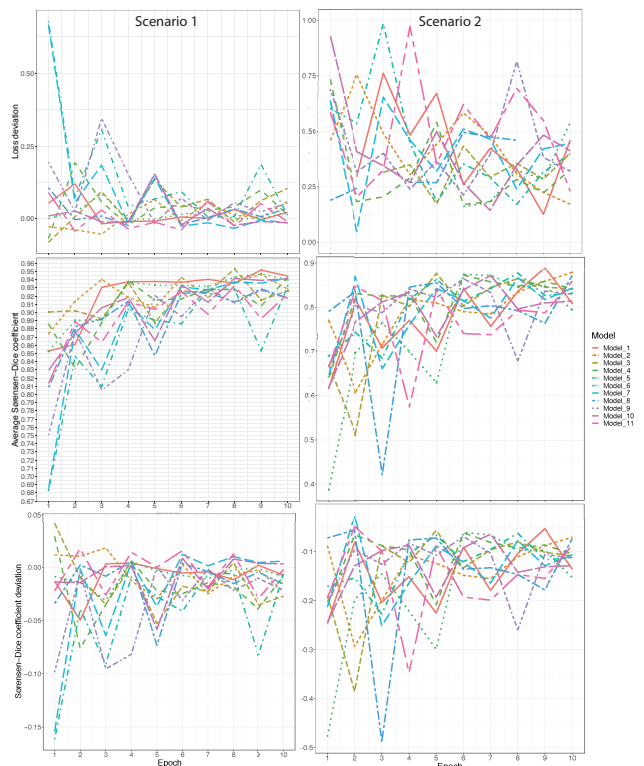


Fig. 3. illustrates plots for evaluation metrics on validation set for 11 models representing different configuration of the architecture hyperparameters in both scenarios. Here, we can see that the metric volatility is more obvious in the first 5 epochs.



was achieved by the model 1 in both scenarios 1 (DSC: 0.951) and 2 (DSC: 0.888). The absence of the junction point leads to performance penalty up to 1.2% while maintaining the same number of core lanes, the initial filter number, and the depth. Further, having junction points more than the number of core lanes causes a decline in dice coefficient by 1.9%. We also identified that the reduction of core lanes decreased DSC by up to 1.1%. Table 1 listed DSC for each model in both scenarios. Further, results related to post-hoc analyses between these models can be found in the supplement file 2.

The application of data flow compression allowed reduction of the parameter quantities while extracting the most useful features for the classification problem. Figure 4 shows the activation maps of some layers of the different networks. Notably, the fully connected layers had remarkably fewer parameters compared to the number necessary

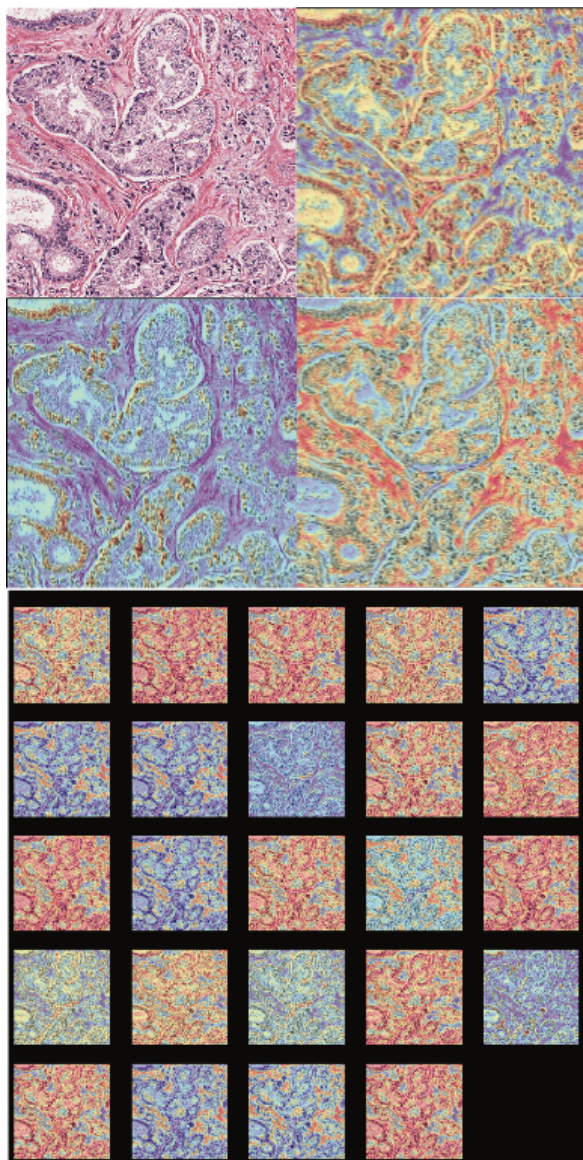


Fig. 4. the image in upper left is the original H&E image. The remaining three activation maps are originated from one of the upper convolutional layers of PlexusNet. Below these images, the activation maps from one of the lower convolutional layers with 24 channels are presented. Red: high value, Blue: low value.

TABLE 1  
HYPERPARAMETER CONFIGURATION AND CLASSIFICATION PERFORMANCE OF EACH MODEL.

Model	Hyperparameters					Dice Coefficient (DSC)	
	Initial Filter	Core lanes	Depth	The number of junction points	Compression rate	Scenario 1 Best DSC Mean (95% CI)	Scenario 2 Best DSC Mean (95% CI)
Model 1	2	5	7	5	0.5	<b>0.952</b> 0.923 (0.898-0.948)	<b>0.888</b> 0.774 (0.716 - 0.820)
Model 2	2	3	7	5	0.5	0.946 0.922 (0.907 - 0.938)	0.877 0.786 (0.730-0.841)
Model 3	2	2	5	5	0.5	0.952 0.916 (0.902 - 0.931)	0.875 0.788 (0.707 - 0.868)
Model 4	2	5	5	5	0.5	0.942 0.908 (0.885 - 0.932)	0.871 0.811 (0.759 - 0.863)
Model 5	2	5	7	3	0.5	0.947 0.920 (0.898 - 0.942)	0.873 0.741 (0.634 - 0.848)
Model 6	2	5	5	5	0.5	0.932 0.867 (0.812 - 0.920)	0.876 0.80 (0.749 - 0.847)
Model 7	2	5	7	7	0.5	0.942 0.886 (0.829 - 0.942)	0.869 0.789 (0.732 - 0.846)
Model 8	2	5	7	1	0.5	0.929 0.895 (0.867 - 0.923)	0.870 0.778 (0.685 - 0.870)
Model 9	2	2	7	1	0.5	0.929 0.876 (0.833 - 0.920)	0.863 0.795 (0.746 - 0.844)
Model 10	2	2	7	2	0.5	0.941 0.906 (0.879 - 0.933)	0.870 0.789 (0.738 - 0.840)
Model 11	2	2	7	0	0.5	0.933 0.895 (0.870 - 0.921)	0.858 0.765 (0.701 - 0.829)

The Dice coefficients (DSC) for each model were estimated on the validation set in Scenario 1 and 2. Scenario 1 includes training and validating a model on training and validation sets that have similar data distribution, whereas scenario 2 the models were trained and evaluated on two different data distributions (Training set is from TCGA-PRAD histology images and the validation set is originated from Stanford's histology images). CI: Confidence interval. Bold text denotes the best DSC.

TABLE 2  
THE NUMBER OF PARAMETERS IN EACH MODEL AND THE POST-HOC ANALYSIS FOR DICE COEFFICIENT COMPARISON FOR TWO SCENARIOS.

Model	Number of Parameters	Best Dice coefficient	The dice coefficient curve of the given model on validation set is not significantly different from*
<b>Scenario 1</b>			
NASNetMobile	5,877,910	0.696	None
MobileNet	4,095,554	<b>0.897</b>	Inception V3 - last layers fixed-, DenseNet 121
Inception V3 -first layers fixed-	26,003,234	0.345	None
Inception V3 - last layers fixed-	26,003,234	<b>0.878</b>	MobileNet, DenseNet 121
DenseNet 121	8,612,930	0.762	MobileNet, Inception V3 - last layers fixed.
PlexusNet	451,220	<b>0.893</b>	None
<b>Scenario 2</b>			
NASNetMobile	5,877,910	0.677	Inception V3 -first layers fixed-, DenseNet 121
MobileNet	4,095,554	<b>0.795</b>	
Inception V3 -first layers fixed-	26,003,234	0.339	NASNetMobile, DenseNet 121
Inception V3 - last layers fixed-	26,003,234	<b>0.866</b>	PlexusNet
DenseNet 121	8,612,930	0.661	Inception V3 -first layers fixed-, DenseNet 121
PlexusNet	451,220	<b>0.888</b>	Inception V3 - last layers fixed-

Evaluation of top three models at slide levels using models trained from Scenario 2 and validated on 8 WS H&E images from Stanford.

Best Models	Mean Dice Coefficient (Range)	Mean AUC (Range)
PlexusNet	0.866 (0.769- 0.963)	0.951 (0.910- 0.992)
Inception V3 - last layers fixed-	0.823 (0.649- 0.998)	0.956 (0.914- 0.998)
MobileNet	0.771 (0.559- 0.984)	0.941 (0.897- 0.986)

More details related to the Post-hoc analysis can be found in the supplement file 3. \* denotes that non-significance of the variation is determined when adjusted  $P$ -value  $\geq 0.05$ .

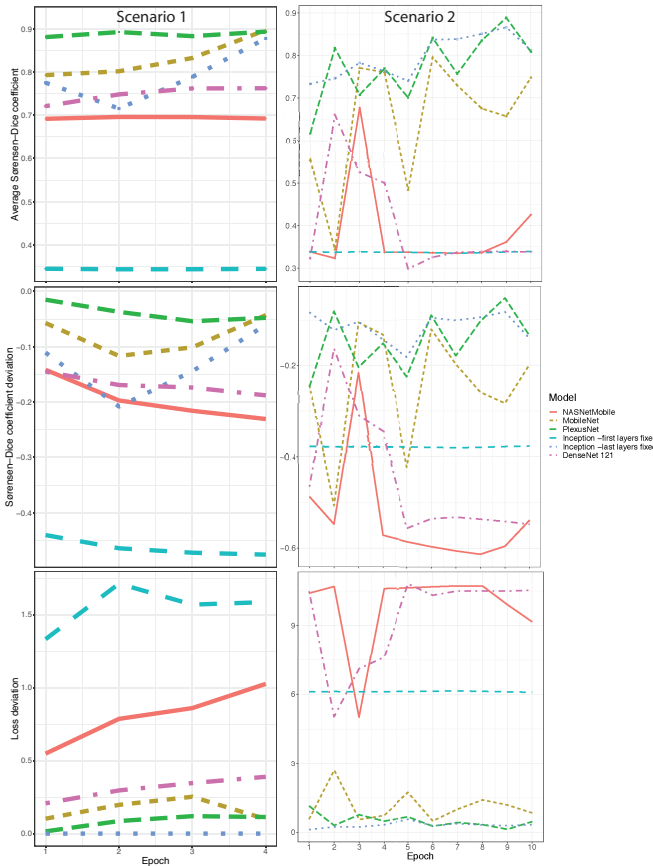


Fig. 5. The curve plots for average dice-coefficient on validation set, its deviation and the deviation in loss values of the validation set from the training set for different model architectures and the PlexusNet in each scenario.

for achieving similar accuracy using state-of-art architectures (e.g., Inception V3, MobileNet). PlexusNet also required 3,223 times less input data (i.e., patch image) to train to a stable model (786,432 data points to 244 data points) compared to the existing architectures. By reviewing the activation maps in different layers in PlexusNet, we found that our novel model focused primarily on features related to nuclear structure and features of the epithelial and stromal compartments to distinguish cancer from non-cancer (Figure 4).

Compared to Inception and MobileNet PlexusNet achieved nearly identical the classification performance parameters with fare fewer parameters (Table 2) demonstrating that PlexusNet learns the most useful features for histological classification of cancer and non-cancer in a shorter epoch period. Furthermore, the discrepancy in DSC between the training and validation sets were lowest with PlexusNet, given that training set and validation set have similar tumor distributions (Figure 5) (The mean difference in DSC between training and validation for PlexusNet: 0.055; for Inception V3: 0.131 and for MobileNet: 0.08). By evaluating the classification accuracy at slide level, all top three models (MobileNet, Inception and PlexusNet) provided similar classification performances in detecting prostate cancer (Table 2).

To test whether PlexusNet was generalizable, we compared its performance in classifying hepatocellular

carcinoma to non-cancerous liver tissues. For this set of experiments, we used PlexusNet models that performed well in prostate cancer histology classification and also included the model with the poorest classification performance as well. Hepatocellular carcinoma was found in 49% of the patch images in the training set, whereas 63% of the validation set of 5 whole-slide images contained cancerous histology. The loss values and the F1-scores were comparable between MobileNet, PlexusNet with the Yogi optimization and Inception in the validation set (Figure 6). However, the dice coefficient of PlexusNet with the Adam optimization significantly varied from that of the Inception model. Overall, our model achieved comparable accuracy in distinguishing hepatocellular carcinoma from non-cancerous liver histologies despite that transfer learning being applied to Inception and MobileNet, whereas PlexusNet was trained from scratch on a relatively small sample size (Table 3).

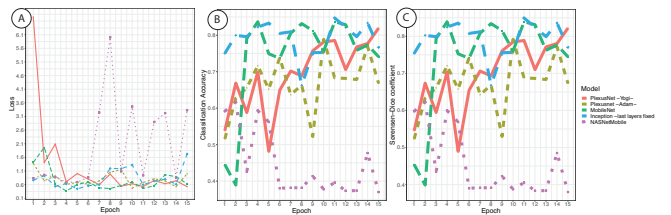


Fig. 6. The curve plots for loss values (A), classification accuracy (B) and Dice coefficient (C) for the state-of-art neural network architecture and the PlexusNet on the validation set from the hepatocellular carcinoma histology image (TCGA-LIHC).

TABLE 3  
PAIRED-WISE POST-HOC ANALYSIS FOR DICE COEFFICIENT BETWEEN DIFFERENT MODELS ON VALIDATION SET FROM HISTOLOGIC IMAGES WITH HEPATOCELLULAR CARCINOMA

Model	Best Dice coefficient (Patch-wise)	Mean Dice coefficient (Range) at slide level (n=5 WS slides)	AUC (Range) at slide level (n=5 WS slides)	The Dice coefficient curve on the validation set differs not significantly* from
PlexusNet - Yogi-	0.822	0.765 (0.761-0.879)	0.814 (0.686-0.885)	PlexusNet -Adam-, MobileNet and Inception V3 -last layers fixed-
PlexusNet - Adam-	0.792	-	-	PlexusNet -Yogi-, MobileNet
MobileNet	0.839	0.729 (0.680 - 0.979)	0.890 (0.136-0.968)	PlexusNet Adam/Yogi, and Inception V3 -last layers fixed-
Inception V3 - last layers fixed-	0.849	0.830 (0.526-0.987)	0.935 (0.856-0.967)	MobileNet and PlexusNet -Yogi-
NASNetMobile	0.622	-	-	None

More details related to the Post-hoc analysis can be found in the supplement file 4. \* denotes that non-significance of the variation is determined when adjusted P-value  $\geq 0.05$ . The mean dice coefficient and AUC (Area Under Curve) were estimated based on 5 H&E WS images from the validation set

## 7 DISCUSSION

The PlexusNet is a novel parallel-lanes convolutional network architecture that facilitates feature extraction with fewer parameters than current convolutional network architectures (in the thousands) for histologic classification problems (Table 2). The activation maps and the results from the evaluation metrics suggest that our novel model

architecture focuses more on learning features that are the most useful for the classification problem. The learning curve and the optimization of the models are regulated by three novel hyperparameters, which also control the parameter capacity of the model. Further, our model achieves classification performance comparable to the state-of-art model architectures with far fewer parameters and the application of transfer learning. Here, the parameter capacity of PlexusNet is 9 or 58 times smaller than that of MobileNet or Inception V3, respectively. PlexusNet can be trained on a single GPU and a batch size of 16 patch images tiled by 512x512 pixels. We failed to train models based on ResNet or DenseNet due to the memory limitation and the need for additional GPU resources for model training purposes.

Given the increased expenses in healthcare services [27-29], a cost-effective solution is required to minimize the cost of health information management. A model that occupies multiple GPUs for training purposes is expensive given the energy and maintaining costs of multiple GPUs. Further, it is more efficient to occupy a single GPU for model training, when there are e.g. more than 100 cancer entities [30] to manage at some time. Besides, there are more than hundreds of different types of disease entities examined during the clinical routine. Thus, there is a need for deep learning models that support efficient management of GPU resources.

Histology images are gigapixel images. Reducing the batch size or downsampling reduces the data flow from histology images (2 or 4 times fewer data flow by halving the batch size or the patch size). Down-sizing is also an issue in pathology image analysis and causes changes in the magnification level. The guidelines for pathology examination are designed by expert opinions [22, 23]. These guidelines provide the magnification levels, at which the evaluation should be performed, support the standardization of pathology examination among the pathologists. The magnification level influences the definition of tumor grading and tumor lesions [22, 23]. We emphasize that the algorithms for cancer detections should meet the standards defined by such guidelines. In our study, 512 pixels correspond to 330  $\mu\text{m}$  at 10x magnification. An image size corresponding to 330x330  $\mu\text{m}$  meets the resolution required for cancer screening on histologic images.

Finally, the demands and the economic aspects of the pathology domain strongly deviate from those of other clinical disciplines like the radiology domain. In general, a pathological evaluation requires a microscope and a qualitative stained histology slide. A microscope usually has a life expectancy of 7-15 years [31]. So, the expense for the device components in the microscopic evaluation is lower compared to other components of the pathology examination that includes the sample processing and the preparation and administration of histology slides. Given that, a cost-effective solution is essential for the successful implementation of a digital pathology system in clinical routine. We believe that PlexusNet can contribute to the development of cost-effective digital pathology evaluation systems.

## 8 CONCLUSIONS

We introduce a novel model architecture called PlexusNet that allows feature extraction and data reduction to develop models for histological classification, in this case, applied to prostate and liver cancer. The model architecture achieves classification performance comparable to the current state-of-art model architecture but requires far smaller training sets and considerably fewer computational resources.

## References

- [1] E. Arvaniti *et al.*, "Author Correction: Automated Gleason grading of prostate cancer tissue microarrays via deep learning," *Sci Rep*, vol. 9, no. 1, p. 7668, May 16 2019.
- [2] M. Lucas *et al.*, "Deep learning for automatic Gleason pattern classification for grade group determination of prostate biopsies," *Virchows Arch*, May 16 2019.
- [3] H. E. Achi *et al.*, "Automated Diagnosis of Lymphoma with Digital Pathology Images Using Deep Learning," *Ann Clin Lab Sci*, vol. 49, no. 2, pp. 153-160, Mar 2019.
- [4] W. Fischer, S. S. Moudgalya, J. D. Cohn, N. T. T. Nguyen, and G. T. Kenyon, "Sparse coding of pathology slides compared to transfer learning with deep neural networks," *BMC Bioinformatics*, vol. 19, no. Suppl 18, p. 489, Dec 21 2018.
- [5] E. Arvaniti *et al.*, "Automated Gleason grading of prostate cancer tissue microarrays via deep learning," *Sci Rep*, vol. 8, no. 1, p. 12054, Aug 13 2018.
- [6] Y. Jiang, L. Chen, H. Zhang, and X. Xiao, "Breast cancer histopathological image classification using convolutional neural networks with small SE-ResNet module," *PLoS One*, vol. 14, no. 3, p. e0214587, 2019.
- [7] G. Campanella *et al.*, "Clinical-grade computational pathology using weakly supervised deep learning on whole slide images," *Nature Medicine*, 2019/07/15 2019.
- [8] G. Litjens *et al.*, "Deep learning as a tool for increased accuracy and efficiency of histopathological diagnosis," *Sci Rep*, vol. 6, p. 26286, May 23 2016.
- [9] T. Falk *et al.*, "U-Net: deep learning for cell counting, detection, and morphometry," *Nat Methods*, vol. 16, no. 1, pp. 67-70, Jan 2019.
- [10] K. Simonyan and A. Zisserman, "Very deep convolutional networks for large-scale image recognition," *arXiv preprint arXiv:1409.1556*, 2014.
- [11] C. Szegedy, V. Vanhoucke, S. Ioffe, J. Shlens, and Z. Wojna, "Rethinking the inception architecture for computer vision," in *Proceedings of the IEEE conference on computer vision and pattern recognition*, 2016, pp. 2818-2826.
- [12] K. He, X. Zhang, S. Ren, and J. Sun, "Deep residual learning for image recognition," in *Proceedings of the IEEE conference on computer vision and pattern recognition*, 2016, pp. 770-778.
- [13] F. Iandola, M. Moskewicz, S. Karayev, R. Girshick, T.



- Darrell, and K. Keutzer, "Densenet: Implementing efficient convnet descriptor pyramids," *arXiv preprint arXiv:1404.1869*, 2014.
- [14] W. Bulten *et al.*, "Epithelium segmentation using deep learning in H&E-stained prostate specimens with immunohistochemistry as reference standard," *Sci Rep*, vol. 9, no. 1, p. 864, Jan 29 2019.
- [15] J. Li *et al.*, "An EM-based semi-supervised deep learning approach for semantic segmentation of histopathological images from radical prostatectomies," *Comput Med Imaging Graph*, vol. 69, pp. 125-133, Nov 2018.
- [16] A. Janowczyk and A. Madabhushi, "Deep learning for digital pathology image analysis: A comprehensive tutorial with selected use cases," *J Pathol Inform*, vol. 7, p. 29, 2016.
- [17] H. Rezaeilouyeh, A. Mollahosseini, and M. H. Mahoor, "Microscopic medical image classification framework via deep learning and shearlet transform," *J Med Imaging (Bellingham)*, vol. 3, no. 4, p. 044501, Oct 2016.
- [18] G. Litjens *et al.*, "Deep learning as a tool for increased accuracy and efficiency of histopathological diagnosis," *Scientific reports*, vol. 6, p. 26286, 2016.
- [19] W. T. Freeman and E. H. Adelson, "The design and use of steerable filters," *IEEE Transactions on Pattern Analysis & Machine Intelligence*, no. 9, pp. 891-906, 1991.
- [20] S. Ioffe and C. Szegedy, "Batch normalization: accelerating deep network training by reducing internal covariate shift," presented at the Proceedings of the 32nd International Conference on International Conference on Machine Learning - Volume 37, Lille, France, 2015.
- [21] M. Trepel, *Neuroanatomie: Struktur und Funktion*. Elsevier, Urban & Fischer, 2012.
- [22] (2019, 07/29/2019). *Surgical Pathology Criteria for Prostatic Adenocarcinoma*. Available: <http://surgpathcriteria.stanford.edu/prostate/adenocarcinoma/grading.html>
- [23] J. Gordetsky and J. Epstein, "Grading of prostatic adenocarcinoma: current state and prognostic implications," *Diagn Pathol*, vol. 11, p. 25, Mar 9 2016.
- [24] K. Zuiderveld, "Contrast limited adaptive histogram equalization," in *Graphics gems IV*, 1994, pp. 474-485: Academic Press Professional, Inc.
- [25] A. Hernández-García and P. König, "Data augmentation instead of explicit regularization," *arXiv preprint arXiv:1806.03852*, 2018.
- [26] M. Zaheer, S. Reddi, D. Sachan, S. Kale, and S. Kumar, "Adaptive methods for nonconvex optimization," in *Advances in Neural Information Processing Systems*, 2018, pp. 9793-9803.
- [27] I. Papanicolas, L. R. Woskie, and A. K. Jha, "Health Care Spending in the United States and Other High-Income Countries," *JAMA*, vol. 319, no. 10, pp. 1024-1039, Mar 13 2018.
- [28] K. Baicker and A. Chandra, "Challenges in Understanding Differences in Health Care Spending Between the United States and Other High-Income Countries," *JAMA*, vol. 319, no. 10, pp. 986-987, Mar 13 2018.
- [29] S. T. Parente, "Factors Contributing to Higher Health Care Spending in the United States Compared With Other High-Income Countries," *JAMA*, vol. 319, no. 10, pp. 988-990, Mar 13 2018.
- [30] (2019, 08/17/2019). *Cancer Types*. Available: <https://www.cancer.gov/types>
- [31] B. E. A. G. SA. (2004, 08/17/2019). *Life span of Biomedical Devices*. Available: <http://cedglobal.org/download/Life%20Span%20of%20Biomedical%20Devices%20-%20Guidance%20Paper%20Final.pdf>